sustainability

IMPACT FACTOR 3.3

CITESCORE 7.7

Article

# A Comparative Study on the Sustainable Remediation of Arsenic Pollution in Water and Soil Using Iron-Modified and Cerium-Modified Biochar

Siyuan Wang, Xiaoxian Yuan, Shifeng Li, Shiji Bie, Yang Zhou, Shuzheng Guo and Zhipu Wang

MDPI

https://doi.org/10.3390/su18062873

*sustainability*

MDPI

*Article*

# A Comparative Study on the Sustainable Remediation of Arsenic Pollution in Water and Soil Using Iron-Modified and Cerium-Modified Biochar

**Siyuan Wang, Xiaoxian Yuan, Shifeng Li, Shiji Bie, Yang Zhou, Shuzheng Guo and Zhipu Wang ***

College of Engineering, China University of Petroleum-Beijing at Karamay, Karamay 834000, China
* Correspondence: 2019592037@cupk.edu.cn; Tel.: +86-0990-6633318

**Abstract**

Arsenic (As) pollution has become a global concern, and the search for effective and sustainable As remediation methods has attracted much attention. Sustainable and cost-effective technologies for As remediation are essential to protect public health. This study aligns with the United Nations Sustainable Development Goals (SDGs), specifically SDG 6 (Clean Water and Sanitation) and SDG 12 (Responsible Consumption and Production), by transforming agricultural waste into value-added biochar for environmental remediation. Currently, studies on the remediation of As pollution using iron-modified biochar (Fe-BC) and cerium-modified biochar (Ce-BC) have demonstrated promising application potential. Although there is an established research foundation regarding their remediation performance and mechanisms, comparative studies evaluating their performance and mechanisms under unified experimental conditions remain limited. As in this study, Fe-BC and Ce-BC were prepared and systematically investigated. The As remediation performance and mechanisms of the two biochars were compared and analyzed through material characterization, aqueous adsorption experiments, and soil remediation assessments. The results showed that the specific surface areas of Fe-BC and Ce-BC were 94.380 $m^2 \cdot g^{-1}$ and 36.388 $m^2 \cdot g^{-1}$, respectively, both higher than that of the original biochar (BC). The Langmuir and Freundlich models adequately fitted the As adsorption processes of all three materials. Fe-BC and Ce-BC exhibited a tendency toward monolayer adsorption for As(III). The Freundlich distribution coefficient $K_F$ of Fe-BC was 0.1604, which was higher than that of BC and Ce-BC, indicating superior adsorption performance for As(III). In the pot experiment, when Fe-BC and Ce-BC were applied at 5%, the As content in ryegrass decreased by 78.38% and 77.15%, respectively. Fe-BC reduced the available As content in soil by 63.1% and decreased As accumulation in ryegrass by 78.38%. The reduction in available As content achieved by Fe-BC was greater than that achieved by Ce-BC. Fe(III) oxides supported on Fe-BC immobilized As through complexation and precipitation mechanisms. $Fe^0$ and $Fe_3O_4$ in the materials altered the redox potential of the local microenvironment, affecting the transformation and stabilization of As species. Ce-BC primarily oxidized As(III) to As(V), and $Ce^{4+}$ facilitated the formation of $CeAsO_4$ precipitates due to its high redox potential.

**Keywords:** arsenic; metal modification; biochar; soil remediation; sustainable remediation



Academic Editor: Luca Di Palma

Received: 8 January 2026
Revised: 3 March 2026
Accepted: 10 March 2026
Published: 14 March 2026



## 1. Introduction

As (As) is widely present in soil and groundwater [1]. Its compounds are classified as Group 1 carcinogens by international cancer research institutions. Long-term exposure

increases the risk of cancer in humans [2]. Inorganic As in soil primarily exists as arsenite (As(III)) and arsenate (As(V)) [3]. As(III) is generally more toxic and mobile than As(V), with toxicity approximately 60 times higher than that of As(V) in aqueous environments. High arsenic concentrations can deteriorate soil physicochemical properties, exert toxic effects on microorganisms, and inhibit plant growth. In aquatic environments, arsenic mainly exists in four oxidation states (−3, 0, +3, and +5), typically as arsenides, elemental arsenic, arsenite, and arsenate species, respectively [4]. Among these species, As(III) is more toxic and mobile than As(V). Inorganic arsenic species are considerably more toxic than organic species [2]. Approximately 220 million people are exposed to arsenic-contaminated drinking water, and more than 105 countries are affected by arsenic pollution [5]. According to the National Soil Pollution Status Survey Principles, the exceedance rate of arsenic in Chinese soils exceeds 2.7%, and nearly 20 million people live in high-risk areas for arsenic exposure [6]. Therefore, remediation of arsenic-contaminated environments is an urgent priority to protect public health, maintain ecological security, and achieve sustainable development.

Porous biochar (BC) has demonstrated significant potential for the remediation of As-contaminated soil, primarily due to its ability to immobilize arsenic through adsorption, electrostatic interactions, and other mechanisms, thereby reducing arsenic leaching and migration [7]. However, several limitations remain in the practical application of pristine biochar. On the one hand, biochar is typically negatively charged and exhibits limited adsorption capacity for anionic arsenic species (such as $AsO_4^{3-}$ and $AsO_3^{3-}$). On the other hand, after application to soil, biochar may release dissolved organic carbon and competitive anions such as $PO_4^{3-}$ and $SO_4^{2-}$, while also increasing soil pH. Consequently, these changes may promote arsenic mobilization and migration, thereby compromising the stability of the remediation effect. To overcome these limitations, metal modification is widely employed to enhance the performance of biochar. After modification, the pore structure of biochar is often optimized, the specific surface area increases, and surface oxygen-containing functional groups (such as –OH and –COOH) become more abundant. These structural changes not only enhance the material's physical adsorption capacity for arsenic but also improve arsenic immobilization through chemical mechanisms such as cation–π interactions, ion exchange, and surface complexation. In particular, metal modification enhances the affinity and selectivity for anionic arsenic species, thereby achieving more stable and efficient arsenic control in complex soil environments [8].

To overcome the limitations of pristine biochar, iron-modified biochar (Fe-BC) and cerium-modified biochar (Ce-BC) have emerged as promising alternatives; however, they operate through distinct mechanisms [9–16]. For instance, Fe-BC immobilizes arsenic through adsorption, coprecipitation, and complexation with iron (hydr)oxides, thereby effectively reducing its mobility and bioavailability, as demonstrated in studies by Wu et al. and Liang et al. [17–20]. In contrast, Ce-BC primarily relies on the oxidation of As(III) to As(V) by high-redox-potential $Ce^{4+}$, followed by precipitation or surface complexation, a key mechanism highlighted by Yu et al. [14]. These fundamental differences in their mechanisms of action suggest that a systematic comparison of their remediation performance is essential to clarify their respective advantages and optimal application scenarios.

However, current knowledge regarding their relative performance remains fragmented because previous studies have predominantly focused on individual materials in simplified aqueous systems. A critical gap exists in the direct and systematic comparison of Fe-BC and Ce-BC within complex soil–plant systems. This lack of side-by-side evaluation limits the development of clear criteria for rational material selection in practical remediation applications.

To address this gap, this study was designed to conduct a comprehensive comparative assessment of Fe-BC and Ce-BC. We aimed to elucidate and compare their adsorption

capacities and mechanisms for As(III) in aqueous solution and to evaluate their relative effectiveness in immobilizing arsenic and reducing its bioavailability in a contaminated soil–plant system. Specifically, this study (1) prepared and characterized Fe-BC and Ce-BC, (2) determined their As(III) adsorption performance and kinetics, and (3) evaluated their efficacy in a ryegrass pot experiment. The novelty of this work lies in its comprehensive side-by-side comparison, systematically evaluating both materials from fundamental adsorption behavior to practical soil remediation performance. This approach provides critical insights for the scenario-specific selection of engineered biochar materials and contributes to sustainable environmental management.

## 2. Materials and Methods

### *2.1. Test Reagents and Instruments*

The reed straw used in this experiment was collected from the lakeside of Hongshan Lake at China University of Petroleum (Beijing), Karamay, China. The reagents used in the experiment were iron oxide ($Fe_2O_3$, AR), cerium nitrate hexahydrate ($Ce(NO_3)_3{\cdot}6H_2O$, REO), sodium arsenite ($NaAsO_2$, RG), and sodium hydroxide (NaOH, GR) (Shanghai Titan Technology Co., Ltd., Shanghai, China). Hexaamminecobalt(III) chloride ($[Co(NH_3)_6]Cl_3$, AR), sodium bicarbonate ($NaHCO_3$, AR), nitric acid ($HNO_3$, AR), hydrofluoric acid (HF, AR), and hydrochloric acid (HCl, AR) were obtained from Chemical Reagent Co., Ltd., Shanghai, China.

The main instruments used in this study are summarized below. For material preparation, an electronic balance (FA2004, Shanghai Lichen Instrument Technology, Shanghai, China), tube furnace (GKD-TF, Shanghai Gaokeda Electric Furnace, Shanghai, China), drying oven (101-1AB, Feisifu Instrument, Huanghua, China), pulverizer (G4510-TD, Dongguan Haode Electric Appliance, Dongguan, China), and vacuum pump (A-i60, Zhejiang Aite Refrigeration Equipment, Taizhou, China) were used. For adsorption experiments and routine analysis, a constant temperature water bath oscillator (SHZ-82A, Changzhou Jintan Renhe Instrument, Changzhou, China), magnetic stirrer (HJ-3B, Hangzhou Jingfei Instrument Technology, Hangzhou, China), pH meter (PH-100pro, Shanghai Lichen, Shanghai, China), and conductivity meter (PHS-25, Shanghai INESA Scientific Instrument, Shanghai, China) were employed. For digestion and elemental determination, a microwave digestion system (YMW-HP100, Changsha Yonglekang Instrument Equipment, Changsha, China) and an inductively coupled plasma optical emission spectrometer (ICP-OES, Agilent 5110, Agilent Technologies, Santa Clara, CA, USA) were utilized.

Material characterization, including scanning electron microscopy (SEM), X-ray diffraction (XRD), Fourier transform infrared spectroscopy (FT-IR), and Brunauer–Emmett–Teller surface area analysis (BET), was performed by external service providers. The specific instrument models were not specified because the analyses were outsourced.

### *2.2. Test Material*

#### 2.2.1. Preparation of Biocarbon Materials

Material pretreatment: The reed straw was washed with deionized water, cut into small pieces, and dried at 60 °C for 48 h. The dried straw was then milled into a fine powder and stored in sealed bags for further use. BC preparation: BC was prepared by pyrolysis. Approximately 100 g of the pretreated straw powder was placed in a quartz boat and pyrolyzed in a tube furnace under an oxygen-free atmosphere (achieved by three cycles of vacuum evacuation). Pyrolysis was conducted at 800 °C for 1 h with a heating rate of 10 $°C{\cdot}min^{-1}$. After cooling to room temperature, the resulting black solid was collected and designated as BC.

Fe-BC preparation: Five grams of $Fe_2O_3$ were mixed with 100 g of the pretreated straw powder, and the mixture was pyrolyzed under the same conditions as BC.

Ce-BC preparation: Ce-BC was synthesized using an impregnation–precipitation method. Briefly, 5 g of $Ce(NO_3)_3 \cdot 6H_2O$ were dissolved in 1 L of deionized water and mixed with 100 g of the pretreated straw powder. The mixture was stirred for 1 h, dried, and then pyrolyzed under the same conditions as BC.

#### 2.2.2. Test Soil

Topsoil samples (0–20 cm) were collected from the vicinity of the F2 experimental building (45°32′39″ N, 84°56′9″ E) on the Karamay campus of China University of Petroleum (Beijing), China. The target arsenic concentration in the artificially contaminated soil was set at 100 $mg \cdot kg^{-1}$, corresponding to the risk control value for agricultural soils with pH > 7.5 specified in the Chinese standard GB 15618–2018.

Preparation of As-contaminated soil: An As(III) stock solution (200 $mg \cdot L^{-1}$) was prepared by dissolving 0.1734 g of $NaAsO_2$ in deionized water adjusted to pH 6.0 to prevent As precipitation and diluting to a final volume of 500 mL. The solution was thoroughly mixed with 1 kg of pretreated soil. The spiked soil was aged in a constant-temperature incubator at 25 °C for 30 days, during which the moisture content was maintained at 60% of the water-holding capacity by periodic addition of deionized water. After aging, the soil was air-dried, ground, and sieved through a 10 mm sieve, resulting in As-contaminated soil with a concentration of 100 $mg \cdot kg^{-1}$.

### *2.3. Test Design*

#### 2.3.1. Adsorption Test

All batch adsorption experiments were conducted in 50 mL centrifuge tubes with a liquid volume of 20 mL. The tubes were shaken in a constant-temperature water bath oscillator at 180 $r \cdot min^{-1}$. The temperature was maintained at 25 ± 0.5 °C (unless otherwise specified) for 24 h. After each experiment, the suspension was filtered through a 0.45 μm membrane filter, and the residual As(III) concentration was determined using ICP-OES (Agilent 5110, Agilent Technologies, USA). All treatments were performed in triplicate.

Adsorption isotherm test: 0.1 g of each biochar (BC, Fe-BC, or Ce-BC) was mixed with 20 mL of As(III) solution at concentrations of 10, 20, 50, 100, and 200 $mg \cdot L^{-1}$ [21].

Adsorption kinetics test: 0.1 g of each biochar was mixed with 20 mL of As(III) solution at a concentration of 200 $mg \cdot L^{-1}$. Samples were collected at 5, 10, 30, and 60 min and at 2, 4, 6, 8, 12, and 24 h.

#### 2.3.2. Influencing Factor Test

pH effect: 0.1 g of each biochar was mixed with 20 mL of As(III) solution at a concentration of 200 $mg \cdot L^{-1}$. The initial pH of the solution was adjusted to 3, 5, 7, 9, and 10 using 0.1 $mol \cdot L^{-1}$ HCl or NaOH.

Temperature effect: 0.1 g of each biochar was mixed with 20 mL of As(III) solution at a concentration of 200 $mg \cdot L^{-1}$. The experiments were conducted at 15 ± 0.5 °C, 20 ± 0.5 °C, 25 ± 0.5 °C, 30 ± 0.5 °C, and 35 ± 0.5 °C.

Effect of material dosage: Different amounts of biochar (0.05, 0.1, 0.15, 0.2, and 0.25 g) were mixed with 20 mL of As(III) solution at a concentration of 200 $mg \cdot L^{-1}$ under standard conditions (25 °C, 24 h).

#### 2.3.3. Phytotoxicity Assay with Ryegrass

A phytotoxicity assay was conducted to evaluate the reduction of arsenic phytotoxicity using ryegrass (*Lolium perenne* L.). The soil was artificially contaminated with As(III) to a target concentration of 100 $mg \cdot kg^{-1}$, as described in Section 2.2.2 (air-dried contaminated

soil). To prevent arsenic leaching, the bottom of each plastic pot was lined with plastic film. A total of 100 g of soil (dry weight) was placed into each pot. BC, Fe-BC, and Ce-BC were thoroughly mixed into the soil at application rates of 1%, 2%, 3%, and 5% (*w*/*w*), equivalent to 1, 2, 3, and 5 g of amendment per 100 g of dry soil, respectively. This design resulted in 15 treatments in total: 3 untreated controls (contaminated soil only) and 12 amendment-treated groups (3 materials × 4 rates). Each treatment was replicated three times (three independent pots), resulting in a total of 45 pots. Ten seeds were sown in each pot. After emergence, the seedlings were thinned to three uniform plants per pot. The pots were watered daily with deionized water to maintain soil moisture at 60% of the field water-holding capacity, adjusted by weight. After a 30-day growth period, the aboveground shoots of ryegrass were harvested, and soil samples were collected from each pot for further analysis.

### *2.4. Analysis Method*

#### 2.4.1. Material Performance Testing and Characterization

Determination of pH and electrical conductivity (EC): Biochar samples were mixed with deionized water at solid-to-liquid ratios of 1:2.5 for pH and 1:5 for EC (m/V). The mixtures were shaken in a constant-temperature water bath oscillator at 180 r·min$^{-1}$ and 25 ± 0.5 °C for 5 min and then allowed to stand for 2 h. The pH and EC of the supernatant were measured using a pH meter (PH-100pro, Shanghai Lichen) and a conductivity meter (PHS-25, Shanghai INESA Scientific Instrument), respectively.

SEM analysis: The morphology of the biochars was observed using SEM. The analysis was performed by an external service provider in Xinjiang, China. Samples were mounted on aluminum stubs with double-sided conductive adhesive tape prior to analysis.

XRD analysis: The crystal structures of BC, Fe-BC, and Ce-BC were identified using XRD. The analysis was conducted by an external service provider in Xinjiang, China. The scan range was set from 10° to 80°, with a scanning rate of 5°·min$^{-1}$, and the total scan time ranged from 11 to 20 min.

FT-IR analysis: The surface functional groups of BC, Fe-BC, and Ce-BC were characterized using FT-IR spectroscopy. The analysis was performed by an external service provider in Xinjiang, China using the standard KBr pellet method. Samples were ground with KBr at an approximate ratio of 1:100 and pressed into transparent pellets. Spectra were recorded in the mid-infrared range (4000–400 cm$^{-1}$) with a resolution of 4 cm$^{-1}$.

BET analysis: The specific surface area, total pore volume, and average pore diameter of the materials were determined using the BET method. The analysis was conducted by an external service provider in Xinjiang, China using nitrogen adsorption–desorption measurements. The degassing temperature was set at 200 °C, and the degassing time was 8 h.

#### 2.4.2. Soil Determination Methods

Soil pH and EC: Soil samples and deionized water were mixed at ratios of 1:2.5 (*w*/*v*) for pH measurement and 1:5 (*w*/*v*) for EC measurement. The suspensions were shaken in a constant-temperature water bath oscillator at 180 r·min$^{-1}$ and 25 ± 0.5 °C for 5 min and then allowed to stand for 2 h. The pH and EC of the supernatant were measured using a pH meter (PH-100pro, Shanghai Lichen) and a conductivity meter (PHS-25, Shanghai INESA Scientific Instrument), respectively.

Determination of total As in soil: Total arsenic was extracted by microwave digestion following the method described in HJ 832–2017 (Chinese standard for soil digestion). Briefly, 0.5 g of air-dried and sieved (<0.15 mm) soil sample was placed in a digestion vessel, and 2 mL of $HNO_3$ and 6 mL of HCl were added. The vessel was placed in a

microwave digestion system and digested according to the program shown in Table 1. After digestion and cooling, the solution was transferred to a 25 mL volumetric flask, diluted to volume with deionized water, and allowed to stand for 60 min. The supernatant was filtered through a 0.45 μm membrane filter, and the arsenic concentration was determined using ICP-OES.

**Table 1.** Temperature rise program for soil microwave digestion.

| Heating Time | Digestion Temperature | Hold Time |
|---|---|---|
| 7 min | room temperature–120 °C | 3 min |
| 10 min | 120–180 °C | 15 min |

Availability of soil As: Available arsenic in soil was extracted using the $NaHCO_3$ method. Briefly, 2 g of air-dried and sieved (<0.15 mm) soil sample was placed in a 50 mL centrifuge tube, and 20 mL of 0.5 mol·$L^{-1}$ $NaHCO_3$ solution (soil-to-solution ratio of 1:10) was added. The mixture was shaken in a constant-temperature water bath oscillator at 180 r·$min^{-1}$ and 25 ± 0.5 °C for 2 h. The suspension was then filtered through a 0.45 μm membrane filter, and the arsenic concentration in the filtrate was determined using ICP-OES (Agilent 5110, Agilent Technologies, USA).

### *2.5. Data Processing and Analysis*

#### 2.5.1. Adsorption Capacity Analysis

The formula for calculating the As adsorption capacity is as follows:

$$q_e = \frac{(C_0 - C_e)V}{m} \quad (1)$$

The formula for calculating the As removal efficiency is as follows:

$$E(\%) = \frac{C_0 - C_e}{C_0} \times 100\% \quad (2)$$

In these equations, $q_e$ (mg·$g^{-1}$) represents the equilibrium adsorption capacity; Ce (mg·$L^{-1}$) is the equilibrium concentration; $C_0$ (mg·$L^{-1}$) is the initial concentration; V (L) is the solution volume; and m (g) is the mass of the adsorbent.

#### 2.5.2. Adsorption Isotherm

The Langmuir adsorption isotherm equation is expressed as follows:

$$q_e = \frac{k_L Q_m C_e}{1 + k_L C_e^n} \quad (3)$$

The Freundlich adsorption isotherm equation is expressed as follows:

$$q_e = k_F C_e^n \quad (4)$$

In these equations, $q_e$ (mg·$g^{-1}$) is the equilibrium adsorption capacity; $q_m$ (mg·$g^{-1}$) is the maximum adsorption capacity of As(III) by biochar; *Ce* (mg·$L^{-1}$) is the equilibrium concentration of As(III) in solution; $k_L$ (L·$mg^{-1}$) is the Langmuir adsorption equilibrium constant; $k_F$ ($mg^{n+1}L^n \cdot g^{-1}$) is the Freundlich adsorption equilibrium constant; and *n* is the Freundlich heterogeneity factor.

#### 2.5.3. Adsorption Kinetics

The pseudo-first-order kinetic equation is expressed as follows:

$$q_t = q_e(1 - \exp(-k_1 t)) \quad (5)$$

The pseudo-second-order kinetic equation is expressed as follows:

$$q_t = \frac{k_2 q_e^2 t}{1 + k_2 q_e t} \quad (6)$$

In these equations, $q_e$ (mg·g$^{-1}$) is the equilibrium adsorption capacity; $q_t$ (mg·g$^{-1}$) is the adsorption capacity at time t; t (min) is the adsorption time; $k_1$ (min$^{-1}$) is the rate constant of the pseudo-first-order model; and $k_2$ (g·mg$^{-1}$·min$^{-1}$) is the rate constant of the pseudo-second-order model.

## 3. Results

### *3.1. Materials Characterization*

#### 3.1.1. Analysis of Physical and Chemical Properties of Biochar

The pH of BC was 10.3, whereas the pH values of Fe-BC and Ce-BC were 8.2 and 8.5, respectively [22]. The EC of pure straw biochar was 905 μs·cm$^{-1}$, while the EC values of Fe-BC and Ce-BC were 1285 and 1337 μs·cm$^{-1}$, respectively.

#### 3.1.2. Characterization and Analysis of Biochar

Figure 1 shows the SEM images of BC, Fe-BC, and Ce-BC. As shown in the figure, the surface of BC was relatively smooth, and the fibrous pore structure retained a relatively intact carbon framework, with scattered shallow circular pores. After modification, both materials exhibited varying degrees of structural alteration, and their microstructures differed significantly. In Fe-BC, the carbon framework was still observable; however, the surface was rough and uneven, with numerous small particles aggregated on it. Ce-BC exhibited a distinct morphology composed of stacked thin sheets, forming an irregular porous structure. This morphology is likely attributed to the agglomeration of cerium oxide nanoparticles driven by their high surface energy during pyrolysis [23]. The surface of Ce-BC contained densely distributed fine particles and exhibited irregular hollow pores.

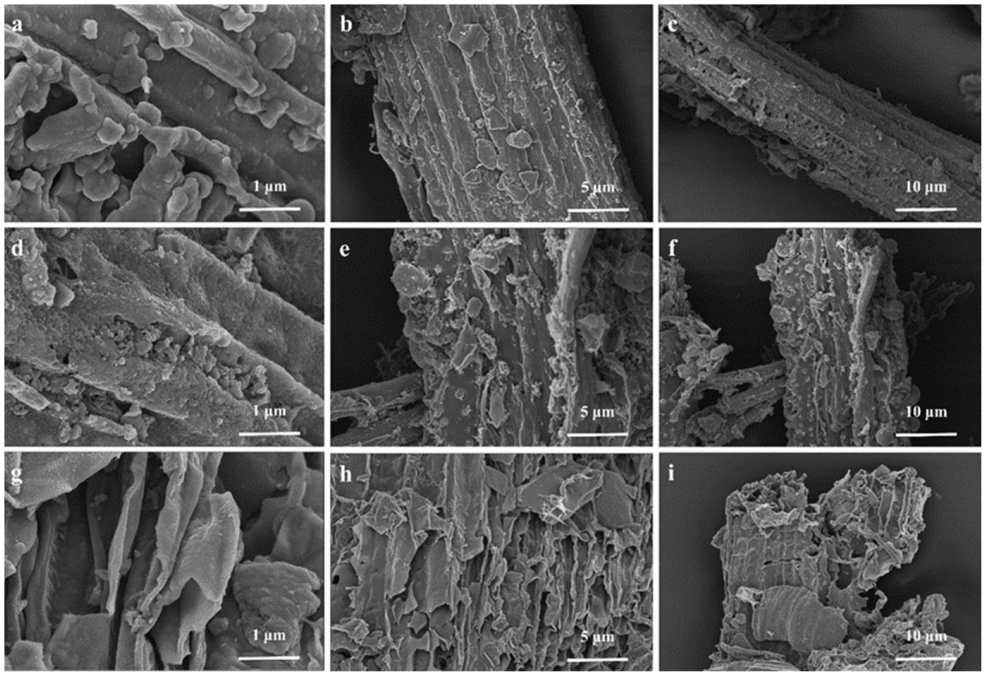


**Figure 1.** SEM images of (**a**–**c**) BC, (**d**–**f**) Fe-BC, and (**g**–**i**) Ce-BC.

The XRD patterns of BC, Fe-BC, and Ce-BC were observed and compared with standard reference data from the PDF-2009 database using JADE 9 software (Figure 2a). Fe-BC

and Ce-BC exhibited diffraction peaks than BC, indicating the successful loading of $Fe_2O_3$ and $CeO_2$ onto the biochar matrix. For BC, a broad diffraction peak corresponding to $sp^3$-hybridized carbon appeared at 2θ = 20–30°, confirming the presence of amorphous carbon [24]. In Fe-BC and Ce-BC, the intensity of the amorphous carbon peak decreased, which may be attributed to the incorporation of metal oxides that reduced the relative diffraction intensity of the carbon phase [25]. For Fe-BC, diffraction peaks observed at 2θ = 39.1° and 73.8° were assigned to $Fe_2O_3$. A peak at 2θ = 46.7° corresponded to $Fe^0$. Diffraction peaks at 2θ = 35.6°, 56.9°, and 62.6° were attributed to $Fe_3O_4$ [26]. Additionally, a diffraction peak corresponding to $Fe_2C$ was detected. For Ce-BC, diffraction peaks at 2θ = 28.4°, 32.9°, 47.4°, 56.5°, and 76.8° were assigned to $CeO_2$ [13].

Figure 2b shows the FT-IR spectra of BC, Fe-BC, and Ce-BC. All materials exhibited a broad absorption band around 3400 $cm^{-1}$, corresponding to O–H stretching vibrations, which was more pronounced in Fe-BC and Ce-BC than in BC. The broad band in the range of 3500–3400 $cm^{-1}$ is attributed to O–H stretching vibrations of hydroxyl (–OH) groups, and its intensity increased significantly after modification [25]. Several weak peaks observed between 3000 and 2900 $cm^{-1}$ correspond to asymmetric C–H stretching vibrations of aliphatic groups [27]. The absorption bands in the range of 1650–1550 $cm^{-1}$ are mainly attributed to C=O and C=C stretching vibrations. The band at 1100–1000 $cm^{-1}$ corresponds to C–O–C stretching vibrations of substituted aromatic rings, while the band at 810–785 $cm^{-1}$ is assigned to aromatic C–H out-of-plane bending vibrations. After modification, the intensities of the C–O–C and aromatic C–H bands became more pronounced [28]. The absorption band at 670–620 $cm^{-1}$ corresponds to Fe–O stretching vibrations, confirming the presence of iron oxides in Fe-BC. Weak bands around 470 $cm^{-1}$ may be associated with Si–O–Si bending vibrations, possibly originating from silica in the original straw feedstock. In Fe-BC, characteristic peaks at 552 $cm^{-1}$ and 891 $cm^{-1}$ were observed, further confirming the presence of $Fe^0$ and oxygen-containing functional groups in the material [29].

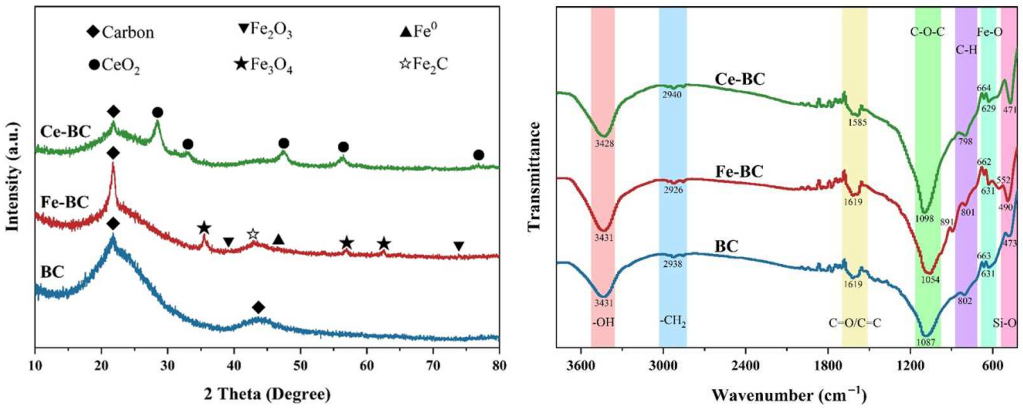


(**a**) (**b**)

**Figure 2.** (**a**) X-ray diffraction patterns of BC, Fe-BC, and Ce-BC; (**b**) FT-IR patterns of BC, Fe-BC, and Ce-BC.

The $N_2$ adsorption–desorption isotherms of BC, Fe-BC, and Ce-BC are presented in Figure 3. All three materials displayed Type IV isotherms with H4 hysteresis loops at $P/P_0 \approx 0.4$–0.8. According to the IUPAC classification, this pattern indicates the presence of slit-shaped mesopores (2–50 nm). The H4 hysteresis loop, which was more pronounced in Fe-BC and Ce-BC than in BC, is characteristic of slit-shaped pores. Its occurrence in the range of $P/P_0 \approx 0.4$–0.8 confirms capillary condensation and evaporation processes, which are defining features of mesoporous structures. The enhanced hysteresis observed in the modified samples suggests that metal–oxygen incorporation restructured the carbon matrix, resulting in a more interconnected mesoporous network compared with the predominantly

microporous structure of BC [30]. This structural evolution directly correlates with the enhanced adsorption capacity (Fe-BC > Ce-BC > BC), as mesopores facilitate faster ion diffusion and provide more accessible surface sites for complexation reactions. This interpretation is further supported by the kinetic results, which demonstrated faster adsorption rates in the modified materials [31].

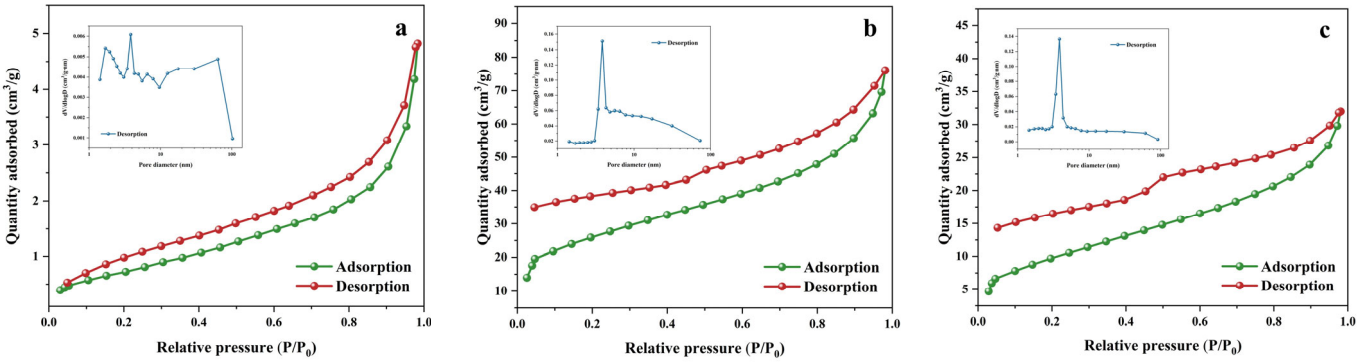


**Figure 3.** (**a**) $N_2$ adsorption–desorption isotherms of BC; (**b**) $N_2$ adsorption–desorption isotherms of Fe-BC; (**c**) $N_2$ adsorption–desorption isotherms of Ce-BC. Inset: the BJH pore size distributions for each sample.

Table 2 lists the specific surface area and pore structure parameters of each material. According to the IUPAC classification, pores with diameters < 2 nm are classified as micropores, those with diameters between 2 and 50 nm are classified as mesopores, and those with diameters > 50 nm are classified as macropores. As shown in Table 2, the average pore diameter of BC was 1.08129 nm, indicating a microporous structure. The average pore diameters of Fe-BC and Ce-BC were 5.43993 nm and 4.98911 nm, respectively, corresponding to mesoporous structures. Mesopores allow the diffusion of larger molecules or ions into the pore network; therefore, mesoporous materials are advantageous for arsenic adsorption. The specific surface area of BC was 2.760 $m^2 \cdot g^{-1}$, whereas the specific surface areas of Fe-BC and Ce-BC were 94.380 $m^2 \cdot g^{-1}$ and 36.388 $m^2 \cdot g^{-1}$, respectively. A substantial number of metal oxide nanoparticles were distributed on the surfaces of Fe-BC and Ce-BC, contributing to the significant increase in specific surface area compared with pristine BC. The increased specific surface area provides more active sites for the adsorption of As(III) and As(V) [24].

**Table 2.** The specific surface area and pore texture parameters of BC, Fe-BC, and Ce-BC.

| Sample Name | BET Surface Area ($m^2 \cdot g^{-1}$) | Total Pore Volume ($cm^3 \cdot g^{-1}$) | Average Pore Size (nm) |
|---|---|---|---|
| BC | 2.760 | 0.98310 | 1.08129 |
| Fe-BC | 94.380 | 0.98105 | 4.98911 |
| Ce-BC | 36.388 | 0.98079 | 5.43993 |

### *3.2. The Adsorption Characteristics of Biochar on As in Water*

#### 3.2.1. Adsorption Isotherm Characteristics

The Langmuir and Freundlich isotherm models were applied to fit the As(III) adsorption data of BC, Fe-BC, and Ce-BC, and the fitting results are presented in Figure 4 and Table 3. As shown in Figure 4, the adsorption capacities of BC, Fe-BC, and Ce-BC for As(III) increased with increasing initial concentration. The adsorption capacities of Fe-BC and Ce-BC were significantly higher than that of BC.

According to Table 3, both the Langmuir and Freundlich models fitted the adsorption data well. The Langmuir model yielded higher correlation coefficients ($R^2$ ranging from 0.9855 to 0.9984), indicating better applicability and suggesting a monolayer adsorption mechanism. The Langmuir constant $K_L$, which reflects adsorption affinity, followed the order Fe-BC (4.9982 $L \cdot mg^{-1}$) > BC (0.0073 $L \cdot mg^{-1}$) > Ce-BC (0.0013 $L \cdot mg^{-1}$), consistent with the stronger chemisorption interactions expected for iron-based materials. The separation factor $R_L$, calculated from the equation $R_L = 1/(1 + K_L C_0)$, ranged from 0.002 to 0.932 for all systems. All $R_1$ values fell between 0 and 1, confirming that the adsorption of As(III) onto BC, Fe-BC, and Ce-BC was a favorable process under the studied conditions, with values closer to 0 indicating stronger adsorption at higher initial concentrations.

The Freundlich constant $K_f$, indicative of adsorption capacity, was 0.1604 for Fe-BC, 0.1582 for BC, and 0.0946 for Ce-BC [32]. The *n* values (0.7009–0.9744) were all below 1, indicating nonlinear adsorption and heterogeneous surface site energies. The superior adsorption performance of Fe-BC can be attributed to its high specific surface area and the abundant iron oxide active sites, which facilitate strong chemical interactions with As(III).

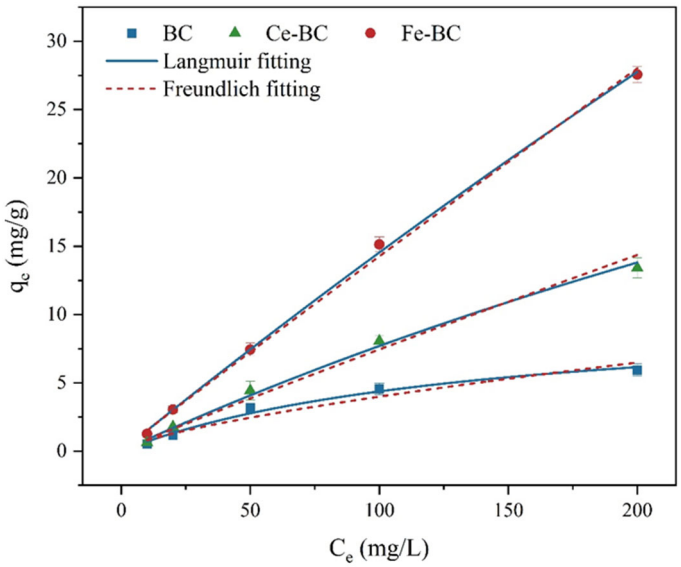


**Figure 4.** Adsorption isotherm curves of As(III) onto BC, Fe-BC, and Ce-BC.

**Table 3.** Equilibrium adsorption isotherm fitting parameters for As(III) onto different adsorbents.

| Adsorbent Material | Langmuir Model | | | Freundlich Model | | |
|---|---|---|---|---|---|---|
| | $Q_m$ ($mg \cdot g^{-1}$) | $k_L$ ($L \cdot mg^{-1}$) | $R_L^2$ | $k_F$ ($L \cdot g^{-1}$) | n | $R_F^2$ |
| BC | 5.95 | 0.0073 | 0.9855 | 0.1582 | 0.7009 | 0.9515 |
| Fe-BC | 27.58 | 4.9982 | 0.9984 | 0.1604 | 0.9744 | 0.9976 |
| Ce-BC | 13.41 | 0.0013 | 0.9926 | 0.0946 | 0.9480 | 0.9875 |

### 3.2.2. Adsorption Kinetics Law

The adsorption kinetic behaviors of BC, Fe-BC, and Ce-BC for As(III) are shown in Figure 5. The adsorption processes of all three materials can be divided into two stages. During the initial stage (0–8 h), BC, Fe-BC, and Ce-BC exhibited rapid adsorption of As(III). After 8 h, the adsorption gradually approached equilibrium. To quantitatively describe the adsorption kinetics, the experimental data were fitted with pseudo-first-order and pseudo-second-order models; the corresponding kinetic parameters are listed in Table 4. As shown in Table 4, the correlation coefficients ($R^2$) of the pseudo-second-order kinetic model for BC, Fe-BC, and Ce-BC were 0.99802, 0.99602, and 0.99614, respectively, which are higher

than those of the pseudo-first-order model (0.99238, 0.99549, and 0.99213, respectively). The adsorption data showed a better fit to the pseudo-second-order kinetic model, suggesting that the rate-limiting step in As(III) removal was more consistent with chemisorption mechanisms involving interactions between the adsorbent surface and arsenic species [33].

Furthermore, the theoretical equilibrium adsorption capacities ($q_e$) calculated from the pseudo-second-order model were 28.12 $mg \cdot g^{-1}$ for Fe-BC, 13.68 $mg \cdot g^{-1}$ for Ce-BC, and 5.98 $mg \cdot g^{-1}$ for BC, which are in excellent agreement with the experimental values (27.58, 13.41, and 5.95 $mg \cdot g^{-1}$, respectively). In contrast, the pseudo-first-order model gave relatively lower calculated values. This consistency further confirms the applicability of the pseudo-second-order model and reaffirms the dominant role of chemisorption.

The pseudo-second-order rate constants ($k_2$) further reflect the distinct adsorption behaviors among the three materials. BC exhibited the highest $k_2$ (0.0028 $g \cdot mg^{-1} \cdot min^{-1}$), indicating rapid initial adsorption despite its low capacity, consistent with a physical adsorption-dominated process. Fe-BC showed the lowest $k_2$ (0.0015 $g \cdot mg^{-1} \cdot min^{-1}$), confirming that its high adsorption capacity arises from slower chemisorption steps, such as surface complexation and precipitation. Ce-BC displayed an intermediate $k_2$ (0.0022 $g \cdot mg^{-1} \cdot min^{-1}$), suggesting that its oxidation–precipitation mechanism proceeds at a moderate rate. These trends align well with the materials' physicochemical properties: Fe-BC benefits from its large specific surface area (94.380 $m^2 \cdot g^{-1}$) and abundant iron active sites ($Fe_2O_3$, $Fe_3O_4$, and $Fe^0$), while Ce-BC (36.388 $m^2 \cdot g^{-1}$) and BC (2.760 $m^2 \cdot g^{-1}$) have progressively fewer active sites, limiting their adsorption capacity and kinetics.

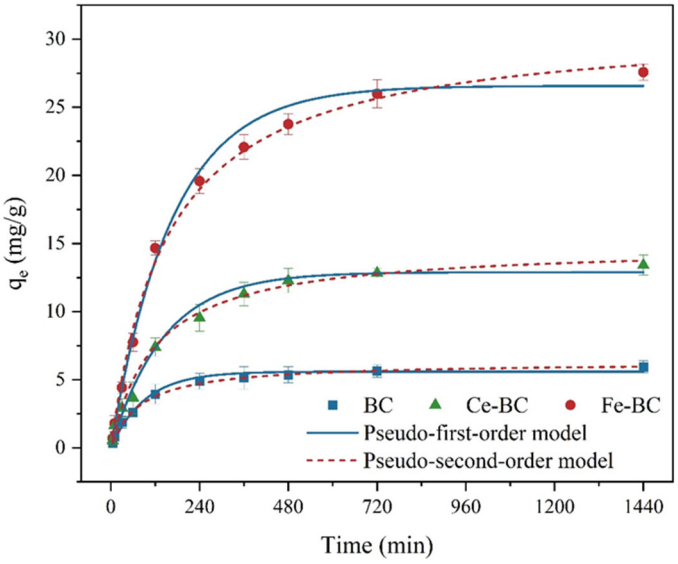


**Figure 5.** Adsorption kinetic model curves of As(III) onto BC, Fe-BC, and Ce-BC.

**Table 4.** Kinetic parameters for As(III) adsorption onto BC, Fe-BC, and Ce-BC.

| Adsorbent Material | Pseudo-First-Order Model | | | Pseudo-Second-Order Model | | |
|---|---|---|---|---|---|---|
| | $q_e$ ($mg \cdot g^{-1}$) | $k_1$ ($min^{-1}$) | $R^2$ | $q_e$ ($mg \cdot g^{-1}$) | $k_2$ ($g \cdot mg^{-1} \cdot min^{-1}$) | $R^2$ |
| BC | 5.72 | 0.0085 | 0.99238 | 5.98 | 0.0028 | 0.99802 |
| Fe-BC | 26.85 | 0.0123 | 0.99549 | 28.12 | 0.0015 | 0.99602 |
| Ce-BC | 12.96 | 0.0098 | 0.99213 | 13.68 | 0.0022 | 0.99614 |

### 3.2.3. Analysis of Other Factors

The initial solution pH affects both the surface protonation of the biochars and the speciation of As(III) in aqueous solution [33]. As shown in Figure 6a, the adsorption

capacities of all three materials increased as the pH increased from 3 to 5, reached a maximum at pH ≈ 5, and then decreased at higher pH values. When pH exceeded 5, the adsorption capacity gradually declined. The maximum adsorption at pH 5 is likely attributed to an optimal balance between two factors: sufficient protonation of surface hydroxyl groups, which facilitates ligand exchange with the predominant neutral As(III) species, $H_3AsO_3$ ($pKa_1$ = 9.2), and minimized competition from hydroxide ions ($OH^-$), whose concentration and competitive effects increase at higher pH values [34]. Surface hydroxyl groups on the materials can form complexes with $H_3AsO_3$, thereby slightly enhancing As(III) adsorption. Under acidic conditions, enhanced surface protonation increases the positive charge density of the materials, facilitating surface complexation with As(III). This effect is associated with pH-dependent changes in surface charge, which influence the availability of active sites. At higher pH values, hydroxide ions compete with As(III) for adsorption sites, resulting in decreased adsorption capacity [35]. Moreover, under alkaline conditions, both the material surface and As(III) species (present mainly as $H_2AsO_3^-$) carry negative charges, leading to electrostatic repulsion and a sharp decline in As(III) removal efficiency. Additionally, BC contains functional groups such as hydroxyl, carboxyl, and amide groups, which may influence interactions with arsenic species and consequently affect adsorption performance. Overall, the primary mechanisms responsible for As removal by BC, Fe-BC, and Ce-BC include ion exchange, electrostatic attraction, surface complexation, redox reactions, and hydrogen bonding [34].

The effect of temperature on As(III) adsorption by BC, Fe-BC, and Ce-BC is shown in Figure 6b. The adsorption capacities of As(III) by BC, Fe-BC, and Ce-BC increased with increasing temperature. Elevated temperature enhances the diffusion rate of arsenic species at the solid–liquid interface, thereby promoting adsorption [35]. The standard enthalpy change (ΔH) values were positive at 15 ± 0.5 °C, 20 ± 0.5 °C, 25 ± 0.5 °C, 30 ± 0.5 °C, and 35 ± 0.5 °C, indicating that the adsorption of As(III) by BC, Fe-BC, and Ce-BC is an endothermic process. The positive ΔH values confirm that increasing temperature favors the adsorption reaction. Thermodynamic analysis further indicates that both physisorption and chemisorption mechanisms may be involved in the removal of As(III) by these biochars. Increasing temperature can activate additional surface adsorption sites and reduce mass transfer resistance, thereby enhancing the adsorption process [36]. The effect of biochar dosage on As(III) adsorption by BC, Fe-BC, and Ce-BC is shown in Figure 6c. As the biochar dosage increased from 0.05 to 0.1 g, the adsorption capacity of As(III) increased for all three materials [37]. At each dosage level, the adsorption capacity followed the order Fe-BC > Ce-BC > BC. When the dosage reached 0.1 g, the adsorption capacities were the highest: 27.58 ± 0.59 $mg \cdot g^{-1}$ for Fe-BC, 13.41 ± 0.73 $mg \cdot g^{-1}$ for Ce-BC, and 5.95 ± 0.46 $mg \cdot g^{-1}$ for BC (Figure 6c).

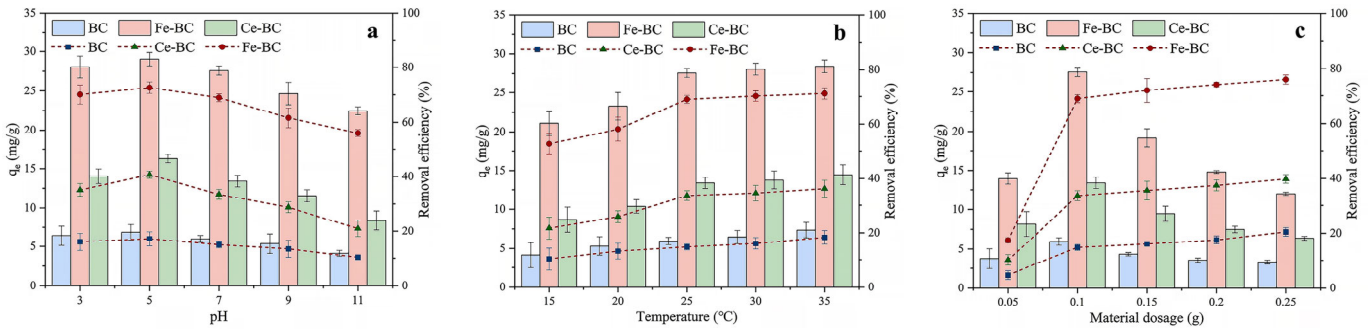


**Figure 6.** (**a**) Effects of pH on As(III) adsorption by BC, Fe-BC, and Ce-BC; (**b**) Effects of temperature on As(III) adsorption by BC, Fe-BC, and Ce-BC; (**c**) Effects of material dosage on As(III) adsorption by BC, Fe-BC, and Ce-BC.

### *3.3. The Passivation Effect of Biochar on As in Soil*

#### 3.3.1. The Effect of Biochar on Ryegrass Yield and Soil Physicochemical Properties

Without any amendment, ryegrass yield was low. The addition of BC, Fe-BC, and Ce-BC increased both the germination rate and biomass of ryegrass. Among the treatments, the highest ryegrass yield was observed with 5% Ce-BC application. This improvement may be attributed to the sustained release of nutrients from the biochars, enhanced soil moisture retention, and improved soil element cycling, increased cation exchange capacity, and reduced nutrient loss [17]. Table 5 presents the physicochemical properties of the soil after the application of different proportions of biochar. The pH of the original soil was 8.1. After the addition of BC, Fe-BC, and Ce-BC, the soil pH increased. The improvement in soil physicochemical properties following the application of the three materials provided favorable conditions for ryegrass growth and stability. BC, Fe-BC, and Ce-BC are alkaline and contribute to buffering adverse soil conditions that may initially inhibit plant growth, thereby significantly increasing soil pH [38]. The EC of the original soil was 2152 $\mu s \cdot cm^{-1}$. The addition of BC, Fe-BC, and Ce-BC significantly affected soil EC, resulting in a decrease compared with the control soil. The reduction in soil EC after biochar application can be attributed to two factors. First, biochar typically contains relatively low levels of soluble salts and therefore does not introduce substantial additional salts into the soil. Second, the porous structure and high specific surface area of biochars enable the adsorption of ions such as $Na^+$ and $Cl^-$, thereby reducing the salt concentration in the soil solution. Second, the porous structure and high specific surface area of the biochars enable them to adsorb ions such as $Na^+$ and $Cl^-$, thereby reducing the salt concentration in the soil solution.

**Table 5.** The physicochemical properties of soil after the application of different rates of BC, Fe-BC and Ce-BC.

| Addition Ratio | Material | pH | EC |
|---|---|---|---|
| 0% | / | 8.1 | 2152 |
| 1% | BC | 8.7 | 1573 |
| | Fe-BC | 8.1 | 1543 |
| | Ce-BC | 8.2 | 1485 |
| 2% | BC | 8.7 | 1413 |
| | Fe-BC | 8.1 | 1318 |
| | Ce-BC | 8.2 | 1390 |
| 3% | BC | 8.8 | 1383 |
| | Fe-BC | 8.2 | 1364 |
| | Ce-BC | 8.2 | 1117 |
| 5% | BC | 8.9 | 1264 |
| | Fe-BC | 8.2 | 1198 |
| | Ce-BC | 8.3 | 1023 |

#### 3.3.2. The Effect of Biochar on Total As in Soil

Figure 7 shows the total arsenic content in soil after different treatments. In the control group (without biochar addition), the total As content was 98.36 ± 1.09 $mg \cdot kg^{-1}$. The lowest total As contents were observed at the 5% application rate for all three biochars, with values of 93.45 ± 3.11 $mg \cdot kg^{-1}$ for BC, 91.78 ± 1.51 $mg \cdot kg^{-1}$ for Fe-BC, and 92.87 ± 3.23 $mg \cdot kg^{-1}$ for Ce-BC. Overall, Fe-BC was more effective than Ce-BC in reducing total soil As at application rates of 1%, 3%, and 5%, whereas Ce-BC showed a slightly greater reduction at the 2% rate. However, because different arsenic species exhibit varying toxicities and mobilities, total arsenic content alone is insufficient to evaluate arsenic bioavailability and toxicity in soil [39]. Oxygen-containing functional groups and

mineral components on the surfaces of BC, Fe-BC, and Ce-BC may form surface complexes or precipitates with arsenic, thereby reducing its mobility. In addition, BC, Fe-BC, and Ce-BC may alter soil redox potential through their redox-active components, facilitating the oxidation of As(III) to As(V) and consequently decreasing arsenic bioavailability.

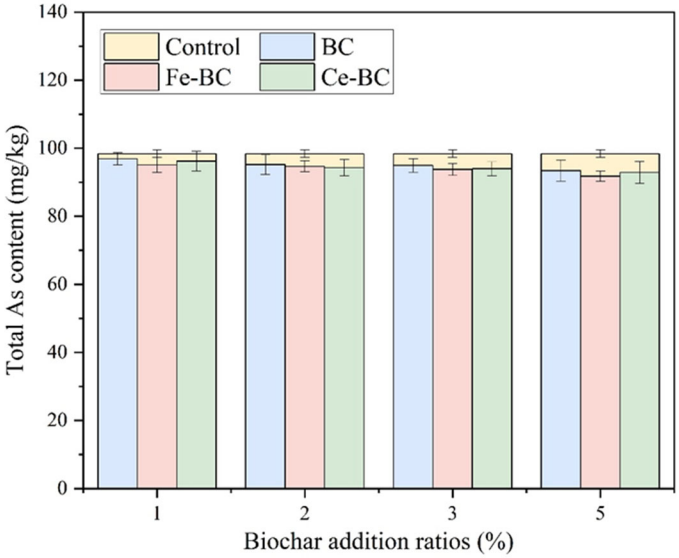


**Figure 7.** Total As content in soil under different application rates of BC, Fe-BC, and Ce-BC.

3.3.3. The Effect of Biochar on Available As in Soil

As in soil primarily exists as inorganic anions (e.g., arsenite and arsenate), which can be adsorbed and immobilized by soil components. Available As represents the fraction that can be directly absorbed by plants and is an important indicator for evaluating arsenic bioavailability in soil. The content of available arsenic is therefore crucial for assessing its environmental risk. Figure 8 shows the available As content in soil under different amendment treatments. The control group received no biochar amendment. As shown in the figure, the available As content in the soil of the control group was $20.95 \pm 2.13$ mg·kg$^{-1}$. At a 5% application rate of BC, Fe-BC, and Ce-BC, the available As content in soil reached the lowest levels, at $9.79 \pm 2.08$ mg·kg$^{-1}$, $7.73 \pm 1.81$ mg·kg$^{-1}$, and $8.31 \pm 2.17$ mg·kg$^{-1}$, respectively. Among the treatments, 5% Fe-BC exhibited the most pronounced reduction in soil available As.

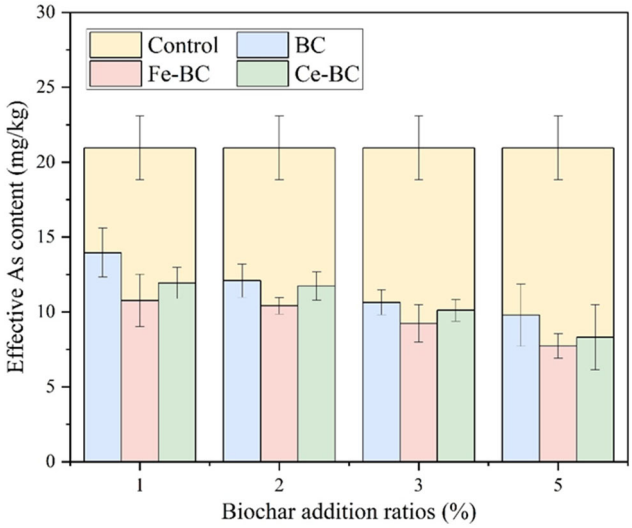


**Figure 8.** Available As content in soil under different application rates of BC, Fe-BC, and Ce-BC.

3.3.4. The Effect of Biochar on As Uptake by Ryegrass

The effects of different biochar amendments on arsenic accumulation in ryegrass are presented in Table 6. As shown in the table, the As content in ryegrass decreased with increasing amendment rate. The As content in ryegrass in the control group was 0.0407 ± 0.001 mg·kg$^{-1}$. When BC, Fe-BC, and Ce-BC were applied at 1%, the As contents in ryegrass were 0.0377 ± 0.0018 mg·kg$^{-1}$, 0.0312 ± 0.0055 mg·kg$^{-1}$, and 0.0348 ± 0.0026 mg·kg$^{-1}$, respectively. At the same application rate, the modified biochar treatments (Fe-BC and Ce-BC) resulted in significantly lower As accumulation in ryegrass compared with BC. Among all treatments, Fe-BC consistently resulted in lower As concentrations in ryegrass than BC and Ce-BC. This effect may be attributed to the higher iron content of Fe-BC, which enhances arsenic immobilization through adsorption and complexation mechanisms. The reduction in As uptake by ryegrass is mainly attributed to the immobilization of arsenic by the biochars through adsorption and surface complexation, thereby decreasing the concentration of bioavailable arsenic in soil. These findings indicate that the addition of modified biochars effectively inhibited arsenic accumulation in ryegrass [27]. When the application rate reached 5%, the As content in ryegrass decreased by 65.6%, 78.38%, and 77.15% for BC, Fe-BC, and Ce-BC, respectively.

**Table 6.** Total arsenic content in ryegrass under different treatment conditions (mg·kg$^{-1}$).

| Material | Total As Content in Ryegrass Under Different Treatment Conditions (mg·kg$^{-1}$) | | | | |
|---|---|---|---|---|---|
| | 0% | 1% | 2% | 3% | 5% |
| BC | 0.0407 ± 0.001 | 0.0377 ± 0.0018 | 0.0338 ± 0.0034 | 0.0306 ± 0.0034 | 0.0140 ± 0.0016 |
| Fe-BC | 0.0407 ± 0.001 | 0.0312 ± 0.0055 | 0.0258 ± 0.0032 | 0.0184 ± 0.0029 | 0.0088 ± 0.0013 |
| Ce-BC | 0.0407 ± 0.001 | 0.0348 ± 0.0026 | 0.0273 ± 0.0047 | 0.0224 ± 0.0042 | 0.0093 ± 0.002 |

## 4. Discussion

### *4.1. Physicochemical Characterization of Metal-Modified Biochars*

Metal modification significantly enhanced the physicochemical properties of biochar by increasing its specific surface area and transforming its pore structure from predominantly microporous to mesoporous, while successfully loading active components such as $Fe_2O_3$ and $CeO_2$ onto the surface (Figure 1 and Table 2). These structural changes constitute the physical basis for the improved adsorption performance. The specific surface areas of Fe-BC and Ce-BC were approximately 34 and 13 times greater than that of BC, respectively. This substantial increase in specific surface area resulted in increasing numbers of physical sites available for arsenic adsorption. Moreover, the enlargement of the average pore diameter into the mesoporous range facilitates the diffusion and transport of As(III) species within the material matrix. This structural transformation effectively overcomes the limited accessibility associated with the predominantly microporous structure of pristine BC [40].

More importantly, metal modification introduces new and highly efficient chemical adsorption sites. The XRD and FT-IR results confirmed the presence of iron and cerium oxides and their corresponding crystalline phases (Figure 2). During the adsorption process, surface hydroxyl groups (≡MOH) on these metal oxides can undergo ligand exchange with arsenate or arsenite species in solution, leading to the formation of stable inner-sphere surface complexes such as Fe–O–As or Ce–O–As [41], which represent the primary mechanism of chemisorption. In addition, modification lowered the point of zero charge ($pH_pzc$) of the materials, as inferred from the decrease in the pH of their aqueous suspensions (from 10.3 for BC to 8.2 for Fe-BC and 8.5 for Ce-BC). This shift indicates altered surface charge characteristics. The adsorption maximum observed at pH ≈ 5 (Figure 6a) can be explained by the balance between two opposing factors. On one hand, this pH provides sufficient

protonation of surface hydroxyl groups to facilitate ligand exchange with the predominant neutral As(III) species, $H_3AsO_3$, which is consistent with the FT-IR evidence. On the other hand, the concentration and competitive effects of hydroxide ions ($OH^-$) remain relatively low at pH = 5 but increase substantially at higher pH values. Consequently, surface complexation dominates the adsorption process under these conditions, whereas electrostatic interactions play a secondary role.

### *4.2. Comparative As Immobilization Mechanisms*

#### 4.2.1. Distinct Chemical Pathways of Fe and Ce Modifiers

For As(III) adsorption, Fe-BC achieved a maximum capacity of 27.58 $mg \cdot g^{-1}$, whereas Ce-BC exhibited 13.41 $mg \cdot g^{-1}$ (Table 3). This pronounced disparity may arise from fundamentally different immobilization pathways governed by their respective metal centers [2,41]. Although Ce-BC outperformed pristine BC, its adsorption capacity remained significantly lower than that of Fe-BC. XRD analysis (Figure 2a) revealed multiple iron phases in Fe-BC, including $Fe^0$, $Fe_2O_3$, and $Fe_3O_4$, each providing distinct reactive sites [42]. The role of $Fe^0$ is particularly noteworthy, as it can act as an electron donor, potentially reducing As(III) to elemental arsenic ($As^0$) or facilitating Fe–As interactions under anoxic conditions [42]. Furthermore, corrosion of $Fe^0$ in aqueous environments generates $Fe^{2+}$ and localized alkaline conditions, which may promote the precipitation of iron (hydr)oxides and subsequent arsenic co-precipitation. Ligand exchange mechanisms, well documented for iron oxide-based adsorbents, are also likely to contribute to arsenic immobilization [41]. $Fe_3O_4$ (magnetite), which contains both $Fe^{2+}$ and $Fe^{3+}$, may facilitate surface-mediated redox reactions, potentially oxidizing As(III) to As(V) while undergoing partial reduction. The resulting As(V) can then be strongly complexed by surface Fe–OH groups [43]. Additionally, heterogeneous interfaces between these iron phases (e.g., $Fe^0/Fe_2O_3$ and $Fe_3O_4/Fe_2O_3$) may create synergistic active sites where electron transfer and arsenic binding are enhanced [42]. This multiphase cooperation likely contributes to the high Langmuir affinity constant ($K_L$ = 4.9982 $L \cdot mg^{-1}$), indicating strong chemisorption behavior, and to an adsorption capacity that surpasses many single-phase iron oxides reported in the literature (Section 4.2.2) [44] (Figure 2a).

In contrast, Ce-BC is primarily characterized by $CeO_2$ (ceria) nanoparticles distributed on the biochar surface (Figure 2a). In $CeO_2$, cerium predominantly exists as $Ce^{4+}$, which possesses a high standard redox potential ($E^\circ$ = 1.61 V for the $Ce^{4+}/Ce^{3+}$ couple). This property enables the oxidation of As(III) to As(V) according to the reaction: $2Ce^{4+} + H_3AsO_3 + H_2O \rightarrow 2Ce^{3+} + H_3AsO_4 + 2H^+$. The generated As(V) may subsequently interact with surface Ce–OH groups or dissolved $Ce^{3+}$, potentially forming cerium arsenate precipitates [13,14]. Although this pathway effectively detoxifies As(III) by converting it to the less mobile As(V) form, it may suffer from two intrinsic limitations: (1) irreversible consumption of active redox sites, as each $Ce^{4+}$ involved in oxidation is reduced to $Ce^{3+}$ and may not be readily reoxidized under ambient conditions; and (2) potential pore blockage by precipitates, which can restrict access to underlying $CeO_2$ sites. These constraints may be reflected in the relatively low Langmuir affinity constant ($K_L$ = 0.0013 $L \cdot mg^{-1}$) and the moderate adsorption capacity of Ce-BC. The single-pathway nature of this mechanism contrasts markedly with the multiphase synergistic behavior observed in Fe-BC, thereby explaining the approximately twofold difference in adsorption capacity. It should be noted that direct spectroscopic evidence for the specific formation of $FeAsO_4$ or $CeAsO_4$ precipitates was not obtained in this study; the proposed mechanisms are inferred from adsorption performance, solution chemistry, and relevant literature [14,41,43,45,46].

#### 4.2.2. Divergent Fixation Pathways in Individually Metal-Modified Biochars

The adsorption capacities observed in this study are consistent with values reported in the literature, thereby providing external support for the proposed mechanisms. A recent review by Sun et al. summarized a wide range of maximum adsorption capacities ($q_m$) for arsenic adsorption onto modified biochars [40]. For iron-modified biochars, reported values typically range from 8.41 $mg \cdot g^{-1}$ for ferrihydrite–bacteria systems to 13.50 $mg \cdot g^{-1}$ for powder formulations [44,47]. The Fe-BC developed in this study (27.58 $mg \cdot g^{-1}$) exceeds these reported values, which is consistent with its multiphase composition that enables synergistic interactions not present in single-phase systems. The internal redox cycling among $Fe^0$, $Fe^{2+}$, and $Fe^{3+}$ may contribute to sustained regeneration of reactive sites, a feature generally absent in simpler iron oxide systems.

For cerium-modified materials, reported adsorption capacities are consistent with the apparent mechanistic limitation observed in this study. Lou et al. [48] reported a maximum adsorption capacity of 10.86 $mg \cdot g^{-1}$ for phosphate adsorption onto Ce-modified biochar, attributing the process primarily to surface precipitation—a mechanism analogous to $CeAsO_4$ formation. The adsorption capacity of Ce-BC in this study (13.41 $mg \cdot g^{-1}$) falls within a comparable range, suggesting that when cerium functions as the sole modifier, adsorption capacity may be intrinsically constrained by the oxidation–precipitation pathway [14]. Although ceria-based materials have been widely reported as effective for the removal of anionic pollutants, their performance for arsenic adsorption appears to be limited by this single dominant mechanism [49].

When placed in the context of advanced multicomponent composites, the trade-off between preparation simplicity and adsorption capacity becomes evident. For example, Fe–Mn–microbe–biochar composites have been reported to achieve a maximum adsorption capacity ($q_m$) of 60.09 $mg \cdot g^{-1}$ [50]. Our side-by-side comparison of individually modified biochars isolates the intrinsic effect of the modifier metal, confirming that the chemical nature of the modifier—and the number of noncompetitive immobilization pathways it enables—are primary determinants of adsorption performance.

These findings suggest an important design principle: biochar composites that incorporate multiple, noncompeting immobilization pathways (e.g., redox reactions, surface complexation, and precipitation) exhibit superior performance compared with materials relying on a single high-affinity mechanism. Iron-based modifications provide this advantage through inherent phase diversity and redox versatility [42,43], whereas cerium-based modifications may benefit from the co-introduction of complementary functional groups or secondary metals to overcome the limitations associated with a single dominant pathway [40].

It should be noted that direct spectroscopic evidence for the specific formation of $FeAsO_4$ or $CeAsO_4$ precipitates was not obtained in this study; the proposed mechanisms are inferred from adsorption performance, solution chemistry, and relevant literature.

### *4.3. Adsorption Dynamics and Thermodynamic Insights*

Building upon the adsorption capacity trends discussed in Section 4.2.2, this section further elucidates adsorption behavior through isotherm modeling and kinetic analysis. The Langmuir model indicates that As adsorption on the surface of modified biochar tends to be uniformly monolayer-covered, and its adsorption sites are homogeneous in energy (Figure 4). The strong fit to the pseudo-second-order kinetic model further suggests that chemisorption is the rate-controlling step of the overall adsorption process, which is consistent with the proposed dominance of chemical mechanisms such as surface complexation and precipitation reactions (Figure 5). Temperature-dependent experiments further demonstrate that the adsorption process is endothermic; therefore, increasing temperature favors arsenic adsorption.

### *4.4. Soil Remediation Efficacy and Environmental Implications*

The results of the pot experiments extend the laboratory-scale adsorption findings to more realistic application scenarios. Fe-BC exhibited the most pronounced effect, reducing soil available arsenic by 63.1% and decreasing arsenic accumulation in ryegrass by 78.38%, which is consistent with its superior adsorption capacity observed in the batch adsorption experiments. This strong passivation effect can be attributed to the synergistic contribution of a mesoporous structure that facilitates mass transfer and iron oxides that provide effective chemical fixation sites [51]. The substantial decrease in soil available arsenic likely reduced arsenic uptake by plant roots, thereby explaining the lower arsenic accumulation in ryegrass [52].

Although Ce-BC showed a slight advantage in increasing ryegrass biomass, Fe-BC played a more decisive role in controlling arsenic bioavailability (Table 5). These findings indicate that reducing pollutant mobility and bioavailability is the primary objective in the remediation of arsenic-contaminated soils. In addition, all modified biochars increased soil pH and decreased EC, which is particularly relevant for alkaline saline soils contaminated with arsenic (Table 4). A moderate increase in soil pH may promote arsenic precipitation with inherent cations such as $Ca^{2+}$ and $Mg^{2+}$, whereas a decrease in EC reduces the concentration of competing anions (e.g., phosphate), thereby indirectly enhancing the specific adsorption of arsenic by the modified materials [53].

### *4.5. Limitations and Future Perspectives*

This study systematically compared the performance of Fe-BC and Ce-BC in the remediation of arsenic pollution. However, similar to many laboratory-scale investigations, it has an inherent limitation: insufficient consideration was given to the post-application stage of the materials. This limitation is reflected in two main aspects: The biochars were not characterized after arsenic adsorption. And the pot experiment lasted only 30 days, after which the biochars remained in the soil, and their long-term behavior was not monitored. These limitations highlight that current understanding of these materials is largely confined to their initial properties, while knowledge of their long-term transformation and end-of-life disposal remains insufficient.

Consequently, how the biochars' surfaces and structures have changed after arsenic adsorption, and what form that arsenic is in. And even if we could answer those questions, the 30-day timeframe of our experiment doesn't really let us predict what might happen years down the line—whether the biochar might degrade, or whether environmental changes could remobilize the arsenic. Addressing these issues is essential for evaluating the long-term stability and sustainability of the remediation performance [54,55].

The purpose of highlighting these limitations is to emphasize that, in practical applications, once biochar is incorporated into soil, it is difficult to recover. Indeed, this challenge has motivated the development of magnetic biochar in recent years [2,56]. After application, biochar becomes integrated into the soil matrix along with the immobilized arsenic. Consequently, direct observation of biochar transformation in soil is difficult; however, indirect insights can be obtained by monitoring changes in the surrounding soil matrix.

Such monitoring should focus on several key aspects: whether soil available arsenic concentrations remain low and stable over time, as an increase may indicate remobilization or loss of passivation effectiveness; whether coexisting anions (such as phosphate and silicate) may progressively compete with arsenic for adsorption sites [57]; whether the optimal pH (≈5) identified under laboratory conditions can be maintained or approximated in alkaline field soils; and how site-specific factors, including soil texture and groundwater flow, influence remediation performance. Addressing these issues is essential for translating laboratory findings into reliable field-scale applications.

Although biochar has demonstrated promising performance over extended periods, the immobilized arsenic does not disappear. Therefore, appropriate end-of-life management strategies must be considered. Existing studies have shown that cement-based materials can effectively immobilize arsenic. Whether through cement solidification to form stable matrices or incorporation into clay bricks, the resulting arsenic leaching concentrations can be reduced below the regulatory thresholds for hazardous waste classification. Recent research further indicates that geopolymer cement systems can effectively stabilize arsenic, primarily through the formation of arsenic-bearing phases such as arsenic-substituted ettringite, calcium arsenate, and iron arsenate compounds. In such systems, the leaching concentration can be reduced to as low as 0.096 $mg \cdot L^{-1}$ after 28 days [58]. The design of these post-remediation management strategies requires a clear understanding of the binding strength between arsenic and biochar and the specific chemical speciation of arsenic. This consideration underscores the importance of post-adsorption characterization. Such analyses, which can elucidate the mechanisms of arsenic immobilization at the material interface, also provide a scientific basis for long-term environmental risk management decisions [7].

The foregoing discussion outlines directions for future research. Post-adsorption characterization and long-term monitoring should not be treated as isolated tasks but rather integrated into the research design from the outset. Batch experiments should routinely include characterization of spent biochars, not only to verify the proposed mechanisms but also to establish a reference framework for subsequent aging studies. The duration of pot experiments should be extended or complemented by field trials to track changes in soil properties and arsenic availability across multiple seasons. Importantly, these efforts should be designed in a coordinated manner so that findings from short-term studies can directly inform the interpretation of long-term observations. Only through such an integrated research framework can the focus shift from merely demonstrating the effectiveness of biochar to understanding its long-term performance and environmental fate.

## 5. Conclusions

To summarize, Fe-BC and Ce-BC exhibited lower intrinsic pH values and higher EC compared with pristine BC. Although the modified biochars themselves had lower pH values, their application to alkaline soil resulted in an overall increase in soil pH, likely due to the release of alkaline components from the biochar matrix. Upon amendment of contaminated soil, these materials increased soil pH and decreased soil EC, thereby improving soil physicochemical properties and reducing arsenic mobility. Characterization results confirmed the successful loading of $Fe_2O_3$ and $CeO_2$ onto BC. Both Fe-BC and Ce-BC exhibited mesoporous structures, and their increased specific surface areas provided additional active sites for arsenic adsorption. The primary mechanisms of arsenic removal by biochar include ion exchange, electrostatic interactions, surface complexation, redox reactions, and hydrogen bonding. The Langmuir model provided a better fit for As(III) adsorption onto the three materials, indicating monolayer adsorption behavior. The adsorption kinetics were better described by the pseudo-second-order model, suggesting that chemisorption was the rate-limiting step. The adsorption capacity followed the order Fe-BC > Ce-BC > BC, with the highest adsorption observed at pH = 5, 35 °C, and a material dosage of 0.1 g. Application of BC, Fe-BC, and Ce-BC increased ryegrass germination rate and biomass, elevated soil pH, and reduced soil EC. At a 5% application rate, both total and available arsenic contents in soil reached their lowest levels, and arsenic concentrations in ryegrass decreased by 65.6%, 78.38%, and 77.15% for BC, Fe-BC, and Ce-BC, respectively.

**Author Contributions:** Conceptualization, S.W. and Z.W.; Methodology, S.W., S.L. and S.G.; Software, X.Y. and Y.Z.; Validation, X.Y. and S.B.; Formal analysis, S.L., S.B. and Z.W.; Investigation, X.Y., S.B. and S.G.; Resources, S.W. and Z.W.; Data curation, X.Y., S.L. and Y.Z.; Writing—original draft, S.W.; Writing—review & editing, X.Y., S.L., S.G. and Z.W.; Visualization, S.B. and Y.Z.; Supervision, Z.W.; Project administration, S.W. and Z.W.; Funding acquisition, Y.Z. and S.G. All authors have read and agreed to the published version of the manuscript.

**Funding:** The study was supported by the Karamay Bureau of Science and Technology under the Karamay Innovative Environment Construction Plan (Innovative Talents) Project (Grant Nos. 2025DB0066 and 2025DB0104).

**Institutional Review Board Statement:** Not applicable.

**Informed Consent Statement:** Not applicable.

**Data Availability Statement:** The datasets used or analyzed during the current study are available from the corresponding author on reasonable request.

**Conflicts of Interest:** The authors declare no conflict of interest.

## Abbreviations

The following abbreviations are used in this manuscript:

| | |
|---|---|
| As | Arsenic |
| SEM | scanning electron microscopy |
| XRD | X-ray diffraction |
| FT-IR | Fourier transform infrared spectroscopy |
| BET | Brunauer–Emmett–Teller surface area analysis |

## References

1. Jiang, X.Y.; Zhang, S.X.; Yin, X.X.; Tian, Y.; Liu, Y.Y.; Deng, Z.W.; Wang, L.H. Contrasting effects of a novel biochar-microalgae complex on arsenic and mercury removal. *Ecotoxicol. Environ. Saf.* **2023**, *262*, 115144. [CrossRef] [PubMed]
2. Amen, R.; Bashir, H.; Bibi, I.; Shaheen, S.M.; Niazi, N.K.; Shahid, M.; Hussain, M.M.; Antoniadis, V.; Shakoor, M.B.; Al-Solaimani, S.G.; et al. A critical review on arsenic removal from water using biochar-based sorbents: The significance of modification and redox reactions. *Chem. Eng. J.* **2020**, *396*, 125195. [CrossRef]
3. Kumarathilaka, P.; Bundschuh, J.; Seneweera, S.; Marchuk, A.; Ok, Y.S. Iron modification to silicon-rich biochar and alternative water management to decrease arsenic accumulation in rice (*Oryza sativa* L.). *Environ. Pollut.* **2021**, *286*, 117661. [CrossRef]
4. Yadav, M.K.; Saidulu, D.; Gupta, A.K.; Ghosal, P.S.; Mukherjee, A. Status and management of arsenic pollution in groundwater: A comprehensive appraisal of recent global scenario, human health impacts, sustainable field-scale treatment technologies. *J. Environ. Chem. Eng.* **2021**, *9*, 105203. [CrossRef]
5. Weerasundara, L.; Ok, Y.-S.; Bundschuh, J. Selective removal of arsenic in water: A critical review. *Environ. Pollut.* **2021**, *268*, 115668. [CrossRef]
6. Chen, W.Z.; Li, M.; Huang, P.Y.; Meng, D.L.; Ying, J.D.; Yang, Y.A.; Qiu, R.L.; Li, H.S. The application of mixed stabilizing materials promotes the feasibility of the intercropping system of Gynostemma pentaphyllum/Helianthus annuus L. on arsenic contaminated soil. *J. Environ. Manag.* **2023**, *348*, 119284. [CrossRef]
7. Ahmed, N.; Tu, P.; Deng, L.; Chachar, S.; Chachar, Z.; Deng, L. Optimizing the dual role of biochar for phosphorus availability and arsenic immobilization in soils. *Sci. Total Environ.* **2024**, *957*, 177810. [CrossRef]
8. Kochar, A.; Al-Juboori, R.A.; Hilal, N. Estrone removal from water through adsorption: A critical review of a decade of research. *J. Water Process Eng.* **2025**, *71*, 107147. [CrossRef]
9. Zhang, D.; Lin, J.; Luo, J.; Sun, S.; Zhang, X.; Ma, R.; Peng, J.; Ji, F.; Zheng, S.; Tian, Z.; et al. Rapid immobilization of arsenic in contaminated soils by microwave irradiation combined with magnetic biochar: Microwave-induced electron transfer for oxidation and immobilization of arsenic (III). *Sci. Total Environ.* **2024**, *919*, 170916. [CrossRef]
10. Jiang, F.; Zhang, C.; Zhang, K.; Luo, H.; Luo, J.; Liu, F. Effect of ascorbic acid and combination with fulvic acid on the electrokinetic remediation of paddy soil contaminated by arsenic-containing acid mine drainage. *Appl. Geochem.* **2023**, *152*, 105632. [CrossRef]
11. Sahu, N.; Singh, J.; Koduru, J.R. Removal of arsenic from aqueous solution by novel iron and iron–zirconium modified activated carbon derived from chemical carbonization of Tectona grandis sawdust: Isotherm, kinetic, thermodynamic and breakthrough curve modelling. *Environ. Res.* **2021**, *200*, 111431. [CrossRef]

12. Bi, X.; Zeng, C.; Westerhoff, P. Adsorption of Arsenic Ions Transforms Surface Reactivity of Engineered Cerium Oxide Nanoparticles. *Environ. Sci. Technol.* **2020**, *54*, 9437–9444. [CrossRef]
13. Wang, Y.; Chen, X.L.; Yan, J.F.; Wang, T.Y.; Xie, X.M.; Yang, S. Efficient removal arsenate from water by biochar-loaded $Ce^{3+}$-enriched ultra-fine ceria nanoparticles through adsorption-precipitation. *Sci. Total Environ.* **2021**, *794*, 148691. [CrossRef]
14. Yu, Y.; Zhang, C.Y.; Yang, L.M.; Chen, J.P. Cerium oxide modified activated carbon as an efficient and effective adsorbent for rapid uptake of arsenate and arsenite: Material development and study of performance and mechanisms. *Chem. Eng. J.* **2017**, *315*, 630–638. [CrossRef]
15. Feng, Y.; Lu, H.; Liu, Y.; Xue, L.; Dionysiou, D.D.; Yang, L.; Xing, B. Nano-cerium oxide functionalized biochar for phosphate retention: Preparation, optimization and rice paddy application. *Chemosphere* **2017**, *185*, 816–825. [CrossRef] [PubMed]
16. Mon, P.P.; Cho, P.P.; Vidyasagar, D.; Ghosal, P.; Madras, G.; Challapalli, S. Synergistic sorption: Enhancing arsenic (V) removal using biochar decorated with cerium oxide composite. *Mater. Today Sustain.* **2024**, *25*, 100675. [CrossRef]
17. Wu, C.; Cui, M.; Xue, S.; Li, W.; Huang, L.; Jiang, X.; Qian, Z. Remediation of arsenic-contaminated paddy soil by iron-modified biochar. *Environ. Sci. Pollut. Res.* **2018**, *25*, 20792–20801. [CrossRef]
18. Liang, M.N.; Lu, L.; Zhang, Q.; Li, J.W.; Qiao, M.S.; Wu, Z.M. Time scale effect of magnetic ferric oxide modified biochar in-situ remediation of arsenic-contaminated paddy soil. *Environ. Technol. Innov.* **2024**, *35*, 103727. [CrossRef]
19. Li, X.N.; Li, R.P.; Zhan, M.Q.; Hou, Q.; Zhang, H.Y.; Wu, G.Q.; Ding, L.Q.; Lv, X.F.; Xu, Y. Combined magnetic biochar and ryegrass enhanced the remediation effect of soils contaminated with multiple heavy metals. *Environ. Int.* **2024**, *185*, 108498. [CrossRef]
20. Tang, L.; Xiong, L.; Zhang, H.; Joseph, A.; Wang, Y.; Li, J.; Yuan, X.; Rene, E.R.; Zhu, N. Reduced arsenic availability in paddy soil through Fe-organic ligand complexation mediated by bamboo biochar. *Chemosphere* **2024**, *349*, 140790. [CrossRef]
21. Azar, M.S.; Raygan, S.; Sheibani, S. Effect of chemical activation process on adsorption of As(V) ion from aqueous solution by mechano-thermally synthesized zinc ferrite nanopowder. *Int. J. Miner. Metall. Mater.* **2020**, *27*, 526–537. [CrossRef]
22. Ottani, F.; Morselli, N.; De Luca, A.; Puglia, M.; Pedrazzi, S.; Allesina, G. The conductivity dilemma: How biochar grain's chemical composition and morphology hinder the direct measurement of its electrical conductivity. *Measurement* **2023**, *222*, 113662. [CrossRef]
23. Rodriguez-Narvaez, O.M.; Peralta-Hernandez, J.M.; Goonetilleke, A.; Bandala, E.R. Biochar-supported nanomaterials for environmental applications. *J. Ind. Eng. Chem.* **2019**, *78*, 21–33. [CrossRef]
24. Wang, G. Simultaneous Immobilization and Mechanisms of Arsenic and Lead in Soil by Sulfur/Iron Modified Biochar. Ph.D. Thesis, East China University of Science and Technology, Shanghai, China, 2022. Available online: https://link.cnki.net/doi/10.27148/d.cnki.ghagu.2022.000002 (accessed on 9 March 2026). (In Chinese)
25. Tan, X. Preparation of Manganese Modified Biochar and Its Remediation Effect on Cadmium and Arsenic Contaminated Soil. Master's Thesis, Beijing University of Chemical Technology, Beijing, China, 2020. Available online: https://link.cnki.net/doi/10.26939/d.cnki.gbhgu.2020.001352 (accessed on 9 March 2026). (In Chinese)
26. Dong, S. Biological Effect and Inactivation of Biochar to Arsenic in Soil. Master's Thesis, Xinjiang Agricultural University, Urumqi, China, 2016. Available online: https://kns.cnki.net/kcms2/article/abstract?v=o8vMLOX1CKs0F-rswWMFZkBt3_k76WO6y1U1c2xzRoU8QrMo1vQAGe-R61JvvHUDzmA7s2CV1y5afumvAwp1a2KlezukIfzbIAFnRHQebslN8tPMqonLjqqpIjl3Qf_5b90uZtAN0bVfx0OLsSd5iuIwEx_ZGjxxRPa9jowqTFQug91demV5mk9h48-UWQ7m&uniplatform=NZKPT&language=CHS (accessed on 9 March 2026). (In Chinese)
27. Yin, X. Effects of Modified Biochar Application on Speciation of Arsenic and Soil Enzyme Activity in Arsenic Contaminated Soil. Master's Thesis, Shandong Agricultural University, Tai'an, China, 2018. Available online: https://kns.cnki.net/kcms2/article/abstract?v=o8vMLOX1CKskxMG8e2aJlJrEPNGryOQ6H4Dfxdq2PTSnK363mbHhRCNVUevNZdWELRMHhUCNCefbVXUGVe7gfgZdSucQlN_nMaSRxJ6Vyk06XXhF7xFgqCdLSsNlUf1QvNw4IC4d7EaTC40dUFop8HBW14mzbi3hKg4B1Vir3cxuHVg-BPV-y7wNnaZCJ7F0&uniplatform=NZKPT&language=CHS (accessed on 9 March 2026). (In Chinese)
28. Xu, M. Effect of Biochar on the Characteristics and Mechanisms of Phosphorus, Arsenic and Chromium Distribution in Soil-Rice System. Ph.D. Thesis, Sichuan Agricultural University, Ya'an, China, 2020. Available online: https://link.cnki.net/doi/10.27345/d.cnki.gsnyu.2020.000047 (accessed on 9 March 2026). (In Chinese)
29. Li, Y. Removal of Cadmium and Arsenic from Water and Soil by Bio-Based Carbon Materials. Master's Thesis, Shandong Agricultural University, Tai'an, China, 2020. Available online: https://link.cnki.net/doi/10.27277/d.cnki.gsdnu.2020.000337 (accessed on 9 March 2026). (In Chinese)
30. Zhu, H.X.; Liu, X.Y.; Jiang, Y.; Zhang, M.; Lin, D.H.; Yang, K. Time-dependent desorption of anilines, phenols, and nitrobenzenes from biochar produced at 700 °C: Insight into desorption hysteresis. *Chem. Eng. J.* **2021**, *422*, 130584. [CrossRef]
31. Maziarka, P.; Wurzer, C.; Arauzo, P.J.; Dieguez-Alonso, A.; Maek, O.; Ronsse, F. Do you BET on routine? The reliability of $N_2$ physisorption for the quantitative assessment of biochar's surface area. *Chem. Eng. J.* **2021**, *418*, 129234. [CrossRef]

32. Lin, L. Effect of Biochar-Ferro Manganese Oxide Composite Material on Bio-Availability of Arsenic. Master's Thesis, Shenyang Agricultural University, Shenyang, China, 2017. Available online: https://kns.cnki.net/kcms2/article/abstract?v=o8vMLOX1CKvt7zz4EAhpNy1VVbbLzcs_pjVk9OtTXppGPgu4o9JiuiJuj_ecRnyIj_yl_JN7mYt-Fh5PvzkfKcbz5J0mNMCWgDrfT7bbT6NczFk_Q-dVitgnWw_7ZF4ToOg-WxVL-EFlbCRY6fH_vsk55Z5HGXhoYIPuyUQAg8Ml7LoCZJrx5VJjpG5Zbmhh&uniplatform=NZKPT&language=CHS (accessed on 9 March 2026). (In Chinese)
33. Li, M. Passivation Effect of Modified Biochar on Cadmium and Arsenic in Polluted Soil. Master's Thesis, Beijing University of Chemical Technology, Beijing, China, 2019. Available online: https://link.cnki.net/doi/10.26939/d.cnki.gbhgu.2019.000376 (accessed on 9 March 2026). (In Chinese)
34. Liang, T. Stabilization Effect and Mechanism Discussion of Cerium-Manganese Modified Wheat Straw Biochar on Arsenic in Soil. Master's Thesis, Chinese Academy of Agricultural Sciences, Beijing, China, 2020. Available online: https://link.cnki.net/doi/10.27630/d.cnki.gznky.2020.000190 (accessed on 9 March 2026). (In Chinese)
35. Din, S.U.; Khaqan, U.; Imran, M.; Al-Ahmary, K.M.; Alshdoukhi, I.F.; Carabineiro, S.A.C.; Al-Sehemi, A.G.; Kavil, Y.N.; Alshehri, R.F.; Bakheet, A.M. Enhancing arsenic removal using Cu-infused biochar: Unravelling the influence of pH, temperature and kinetics. *Chem. Eng. Res. Des.* **2024**, *203*, 368–377. [CrossRef]
36. Lin, L. Effect of Biochar-Metal Oxides Composite Material on Bio-Availability of Arsenic. Ph.D. Thesis, Chinese Academy of Agricultural Sciences, Beijing, China, 2020. Available online: https://link.cnki.net/doi/10.27630/d.cnki.gznky.2020.000039 (accessed on 9 March 2026). (In Chinese)
37. Choudhury, T.R.; Sajib, M.S.H.; Sowrav, S.F.F.; Khan, S.R.; Alam, M.N.E.; Amin, M.N. Nanostructured bi-metallic biochar: An innovative approach for arsenic (III) removal from contaminated water. *Environ. Chem. Ecotoxicol.* **2025**, *7*, 10–18. [CrossRef]
38. Qiu, J.; De Souza, M.F.; Wang, X.L.; Ok, Y.S.; Meers, E. Influence of biochar addition and plant management (cutting and time) on ryegrass growth and migration of As and Pb during phytostabilization. *Sci. Total Environ.* **2024**, *913*, 169771. [CrossRef]
39. Bai, S. Passivation Effect of Hydroxy Sulfate Ironsludge-Based Biochar on Arseniccontaminated Soil. Master's Thesis, Tianjin University of Technology, Tianjin, China, 2019. Available online: https://kns.cnki.net/kcms2/article/abstract?v=o8vMLOX1CKskxMG8e2aJlJrEPNGryOQ6H4Dfxdq2PTSnK363mbHhRKYV54DR80dkz11_uchGVjw9oX31CpGd5Afa7lhB3dAdzbVHBtyg1iqT8TJnl6iCTP72Afe-aRhXM5D2098zxT3LIfsB_nLzNrFeGvap3AIabuHjhKJ8JqQ-CYufmYEJHfKN2Z3IrqlT&uniplatform=NZKPT&language=CHS (accessed on 9 March 2026). (In Chinese)
40. Sun, Y.; Yu, F.; Han, C.; Houda, C.; Hao, M.; Wang, Q. Research Progress on Adsorption of Arsenic from Water by Modified Biochar and Its Mechanism: A Review. *Water* **2022**, *14*, 1691. [CrossRef]
41. Song, B.; Zhi, Z.; Zhou, Q.; Wu, D.; Yu, L.; Gong, F.; Yin, Y.; Meng, F.; Li, C.; Chen, Z.; et al. Enhanced arsenic removal by reusable hexagonal $CeO_2/Fe_2O_3$ nanosheets with exposed (0001) facet. *Sci. Total Environ.* **2022**, *847*, 157490. [CrossRef]
42. Hu, L.; Zhang, P.; Xu, X.; Ren, J.; Zhao, L.; Qiu, H.; Cao, X. Immobilization of arsenic in different contaminated soils by zero-valent iron-embedded biochar: Effect of soil characteristics and treatment conditions. *Sci. Total Environ.* **2023**, *868*, 161597. [CrossRef]
43. Pan, H.; Yang, X.; Chen, H.B.; Sarkar, B.; Bolan, N.; Shaheen, S.M.; Wu, F.C.; Che, L.; Ma, Y.B.; Rinklebe, J.; et al. Pristine and iron-engineered animal- and plant-derived biochars enhanced bacterial abundance and immobilized arsenic and lead in a contaminated soil. *Sci. Total Environ.* **2021**, *763*, 144218. [CrossRef] [PubMed]
44. Cao, R.; Kang, G.D.; Zhang, W.W.; Zhou, J.H.; Xie, W.L.; Liu, Z.Z.; Xu, L.; Hu, F.; Li, Z.; Li, H.X. Biochar loaded with ferrihydrite and Bacillus pseudomycoides enhances remediation of co-existed Cd(II) and As(III) in solution. *Bioresour. Technol.* **2024**, *395*, 130323. [CrossRef] [PubMed]
45. Li, J.; Zu, Y.; Li, G.; Sun, G. Mechanism of As(V) removal from water by lanthanum and cerium Modified Biochars. *Environ. Sci.* **2018**, *39*, 2211–2218. (In Chinese) [CrossRef]
46. Liang, T.; Li, L.F.; Hu, Y.A.; Xu, W.M. Arsenic Immobilization for Paddy Field and Improvement of Rice (*Oryza sativa* L.) Growth through Cerium-Manganese Modified Wheat Straw Biochar Application. *Sustainability* **2023**, *15*, 16161. [CrossRef]
47. Kim, J.; Song, J.; Lee, S.M.; Jung, J. Application of iron-modified biochar for arsenite removal and toxicity reduction. *J. Ind. Eng. Chem.* **2019**, *80*, 17–22. [CrossRef]
48. Lou, L.; Li, W.K.; Yao, H.; Luo, H.Y.; Liu, G.; Fang, J. Corn stover waste preparation cerium-modified biochar for phosphate removal from pig farm wastewater: Adsorption performance and mechanism. *Biochem. Eng. J.* **2024**, *212*, 109530. [CrossRef]
49. Verma, V.; Kumar, N.; Sharma, Y.C. Application of a stabilized bioproduct, ceria-biochar ($CeO_2$/BC), for economic nitrate removal from drinking water. *Biofuels Bioprod. Biorefining* **2026**. Early Access. [CrossRef]
50. Lian, B.; Wu, J.Z.; Bolan, N.; Jeyakumar, P.; Wang, H.L.; Yuan, J.; Wu, Q.C.; Chen, Y.; Wang, J.H.; Yuan, F.; et al. Fe-Mn oxide, microbe and biochar composite for remediation of Cd and As co-contaminated water and soil. *Soil Use Manag.* **2024**, *40*, e13162. [CrossRef]
51. Lu, L.; Yan, L.; Liang, M.; Cheng, G.; Zhu, Z.; Zhu, Y.; Wang, D. Preparation of magnetic iron oxide/mulberry stem biochar and its effects on dissolved organic carbon and arsenic speciation in arsenic-contaminated soils. *Environ. Sci.* **2022**, *43*, 5214–5223. (In Chinese) [CrossRef]

52. Karczewska, A.; Galka, B.; Dradrach, A.; Lewinska, K.; Molczan, M.; Cuske, M.; Gersztyn, L.; Litak, K. Solubility of arsenic and its uptake by ryegrass from polluted soils amended with organic matter. *J. Geochem. Explor.* **2017**, *182*, 193–200. [CrossRef]
53. Gliniak, M.; Sikora, J.; Sadowska, U.; Klimek-Kopyra, A.; Latawiec, A.; Kubo, M. Impact of biochar on soil electrical conductivity during 2 year field experiment. In Proceedings of the 6th World Multidisciplinary Earth Sciences Symposium, WMESS 2020, Prague, Czech Republic, 7 September 2020–11 September 2020; IOP Publishing Ltd.: Bristol, UK; Volume 609, p. LAMA Energy Group; Prague City Tourism; LAMA Gas and Oil. s(V) removal from water. [CrossRef]
54. Cui, Z.W.; Wang, Y.; Wang, N.; Ma, F.F.; Yuan, Y.Y. Effects of Ageing on Surface Properties of Biochar and Bioavailability of Heavy Metals in Soil. *Agriculture* **2024**, *14*, 1631. [CrossRef]
55. Wang, Z.; Geng, C.X.; Bian, Y.; Zhang, G.Y.; Zheng, C.L.; An, C.J. Effect of oxidative aging of biochar on relative distribution of competitive adsorption mechanism of $Cd^{2+}$ and $Pb^{2+}$. *Sci. Rep.* **2022**, *12*, 11308. [CrossRef]
56. Wu, Y.; Wang, Z.W.; Xue, Z.Y.; Yan, Y.H.; Huma, B.; Zhou, Y.Q.; Tan, Z.X. Fertilization of potentially toxic element-contaminated soils remediated with reusable biochar pellets using rice straw, pig manure and their derived biochar. *Environ. Pollut.* **2025**, *366*, 125551. [CrossRef] [PubMed]
57. Liu, H.X.; Xie, X.J.; Wang, Y.X. Selective arsenic removal in complex aquatic environments: Mechanistic insights, sorbent design, and environmental regulation. *J. Hazard. Mater.* **2026**, *501*, 140761. [CrossRef] [PubMed]
58. Li, C.P.; Liu, Y.; Xu, S.T.; Wang, J.S.; Bao, C.J.; Liu, Y.; Zhang, Z.F.; Bin, Y.J.; Liu, D.W. Study on the remediation of arsenic pollution in tin tailings by Geopolymer-cementitious hybrids. *Miner. Eng.* **2025**, *232*, 109546. [CrossRef]